Smart Structures and Systems, *Vol. 24, No. 1 (2019) 15-26*
DOI: https://doi.org/10.12989/sss.2019.24.1.015

Enhance the damping density of eddy current and electromagnetic dampers

Jin-Yang Li[1], Songye Zhu[*1,2] and Jiayang Shen[1]

[1]*Department of Civil and Environmental Engineering, The Hong Kong Polytechnic University, Hong Kong, China*
[2]*The Hong Kong Branch of National Rail Transit Electrification and Automation Engineering Technology Research Center, The Hong Kong Polytechnic University, Hong Kong, China*

(Received February 28, 2019, Revised March 8, 2019, Accepted March 10, 2019)

Abstract. Over the past decades, a great variety of dampers have been developed and applied to mechanical, aerospace, and civil structures to control structural vibrations. This study is focused on two emerging damper types, namely, eddy current dampers (ECDs) and electromagnetic damper (EMDs), both of which are regarded as promising alternatives to commonly-applied viscous fluid dampers (VFDs) because of their similar mechanical behavior. This study aims to enhance the damping densities of ECDs and EMDs, which are typically lower than those of VFDs, by proposing new designs with multiple improvement measures. The design configurations, mechanisms, and experimental results of the new ECDs and EMDs are presented in this paper. The further comparison based on the experimental results revealed that the damping densities of the proposed ECD and EMD designs are comparable to those of market-available VFDs. Considering ECDs and EMDs are solid-state dampers without fluid leakage problems, the results obtained in this study demonstrate a great prospect of replacing conventional VFDs with the improved ECDs and EMDs in future large-scale applications.

Keywords: damping density; electromagnetic damper; eddy-current damper; viscous fluid damper; ball screw

1. Introduction

A great variety of dampers operating in passive, semi-active or active modes have been developed and applied to vibration mitigation/suppression of mechanical, aerospace, and civil structures. Viscous fluid dampers (VFDs), usually consisting of pistons immersed in viscous fluid (such as silicone or oil), are one of the most widely accepted types of passive dampers (Housner *et al*. 1997). A VFD generally produces a damper force that is linearly proportional or nonlinearly correlated to the relative velocity of the damper. It can enhance the damping of a structure by dissipating structural vibration energy.

Recently, two emerging types of passive dampers, namely, eddy current dampers (ECDs) and electromagnetic dampers (EMDs), have received growing interest in the field of vibration mitigation. Both types take advantage of the electromagnetic induction effect that produces an electromotive force (*emf*) given a changing magnetic field and thus enables the conversion between kinetic and electric energy. Their principles are briefly introduced as follows.

An ECD comprises permanent magnets and conductive materials with relative motions to each other. The changing magnetic flux generates eddy currents (also known as Foucault currents) in the conductive materials, and in turn the eddy currents develop a repulsive force within the magnetic field. Consequently, an ECD produces a damping force that is proportional to the damper velocity and against the relative motion of the damper. Compared with traditional VFDs, ECDs are associated with the following advantages:

- ECDs are solid-state dampers and can avoid the leakage problem associated with common VFDs (Sodano and Bae 2004).
- The magnets and conductive materials with relative motions can be designed to be non-contact. Thus ECDs can minimize the abrasion due to friction (Sodano and Bae 2004) and demonstrate robust and durable performance (Ebrahimi *et al*., 2009).

ECDs has been applied in magnetic braking systems for decades (Heald 1988, Lee and Park 1999, Simeu and Georges 1996, Wiederick *et al*. 1987). Recently, the applications of ECDs have been extended to vibration control. For example, ECDs were proven effective in controlling vibrations of cantilever beams (Bae *et al*. 2005, Sodano *et al*. 2005). Wang *et al*. (2012) conducted a feasibility test on a tuned mass damper (TMD) system containing ECD; the experimental results revealed its satisfactory control performance, durability, and economic viability of the system. Lu *et al*. (2017) analyzed the performance improvement of a supertall building using TMD plus ECD. Niu *et al*. (2018) demonstrates the application of ECD to vibration control of bridge hangers.

An EMD is essentially a common electromagnetic (EM) device comprising permanent magnets and coil windings. The relative motions between the permanent magnets and coils generate a back *emf* (voltage) in the coils. However, the *emf* generates the current only if two ends of the coils are connected to a closed circuit. Consequently, an EMD converts kinetic energy into electric energy, and then shunts the electric energy into external circuits. The beauty of EMD is that its mechanical behavior is governed by the

*Corresponding author, Associate Professor
E-mail: songye.zhu@polyu.edu.hk

 ISSN: 1738-1584 (Print), 1738-1991 (Online)

external shunt circuit, enabling the complex design of damper behavior. Several appealing functions of EMDs have been explored in the literature:
- An EMD connected to a specially designed shunt circuit is often referred to as an electromagnetic shunt damper (EMSD). Thanks to the analogous relationship between electrical and mechanical systems, EMSDs can mimic versatile damper types (including VFDs, visco-elastic dampers, inerter dampers, etc.), by simply manipulating the external circuits (Li and Zhu 2018, Smith 2002).
- By connecting an energy harvesting circuit, an EMD can be designed to fulfill vibration damping and energy harvestings functions simultaneously (Zhu *et al*. 2012). In addition to the benefit of extra energy harvesting, this strategy avoids the overheating problem of the damper by converting kinetic energy into electric energy rather than heat.
- A self-powered vibration control and sensing system can be established by integrating the EMD with vibration damping and energy harvesting functions and low-power wireless sensors (Shen *et al*. 2012).

Extensive researches on EMDs or EMSDs have been conducted (Behrens *et al*. 2003, 2005, Cassidy *et al*. 2011, Fleming and Moheimani 2006, Inoue *et al*. 2008, Shen *et al*. 2012, 2016, 2018, Yan *et al*. 2012, Jamshidi *et al*. 2017, Zhu *et al*. 2012, 2019).

Notably, when an EMD is connected to a resistor or a short circuit, the EMD also produces a proportional force vs. velocity relationship. Therefore, given their similar mechanical behaviors, both ECDs and EMDs, which represent two solid-state dampers without using any fluid, can potentially replace conventional VFDs in many applications.

However, compared with conventional VFDs, linear-motion ECDs and EMDs typically have relatively lower damping densities, where damping density is defined as the ratio of the provided equivalent damping coefficient over the damper volume (Palomera-Arias *et al*. 2008)

$$DD = \frac{c_{eq}}{V} \tag{1}$$

where DD denotes the damping density, c_{eq} is the equivalent viscous damping coefficient of the damper, and V is the damper volume. Comparisons and discussions among ECDs, EMDs, and other conventional viscous fluid dampers (VFDs) were made possible by this unified parameter. The low damping density will limit their applications in large-scale civil structures that typically require great damper forces and damping coefficients.

Therefore, this study aims to address this existing limitation of ECDs and EMDs by proposing some improved designs. Various improvement measures were applied to the ECDs and EMDs individually, and their effectiveness were successfully verified through experimental characterization. Furthermore, the damping densities of the improved ECDs and EMDs were compared with those of market-available VFDs, which showed the great prospects of the proposed design in practical applications.

2. Linear-to-rotary conversion setup

In view of the low efficiency of linear-motion ECDs and EMDs, the setup shown in Fig. 1 was adopted in this study to convert linear motions to rotary motions. As a result, rotary-type ECDs and EMDs with relatively high efficiency can be employed to control the linear motion. A similar setup was also used by Nakamura *et al*. (2014) for seismic response control.

A ball screw with a large lead angle was used to transform linear motions into rotary motions, and to accelerate the relative velocity between magnets and conductive materials, thereby producing higher *emf* and larger damping forces in ECDs and EMDs.

A gearbox can further amplify the relative angular velocity by α times, where α stands for the gearbox ratio. Consequently, the relation between the rotation angle of the rotary damper and the linear displacement is

$$\theta_s = \frac{2\pi\alpha}{l} x \tag{2}$$

where l is the ball-screw lead, x is the linear displacement of the input loading shaft, θ_s is the rotation angle of the output shaft, and α is the gear ratio. Meanwhile, a gearbox also amplifies the torque transferred from the rotary damper. Thus, a gearbox can amplify the total damping by a factor of α^2. By selecting appropriate l and α values, the rotation speed can be considerably increased without increasing the total size.

Two conversion setups were employed in the experimental study in the following sections, namely,

Setup I: Ball screw only
Setup II: Ball screw + gearbox

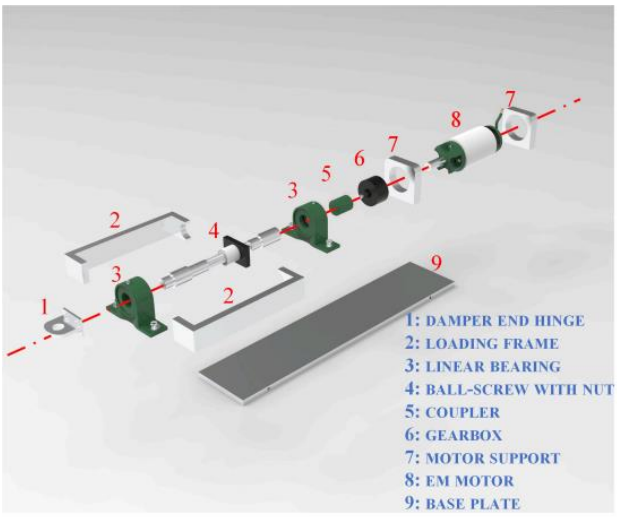

Fig. 1 Exploded view drawing of the proposed rotary type setup (EMD)

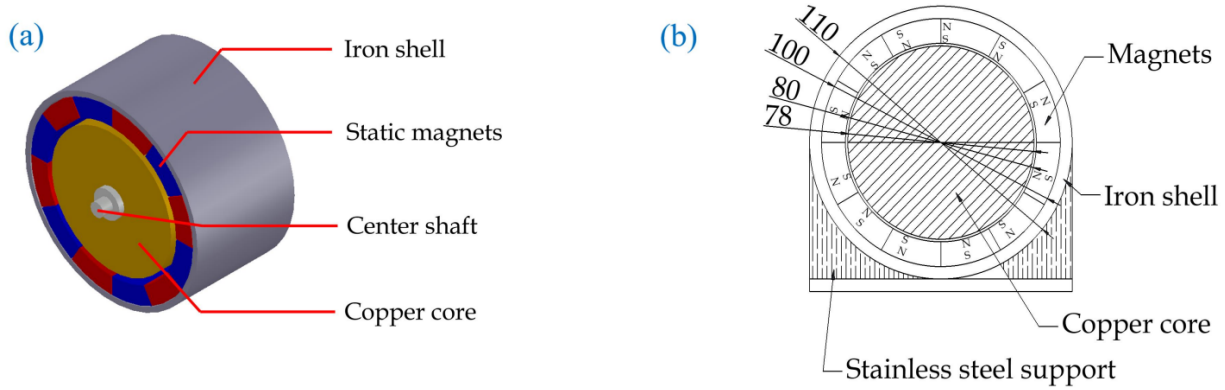

Fig. 2 Configuration of ECD-A: (a) 3D view and (b) cross-section view

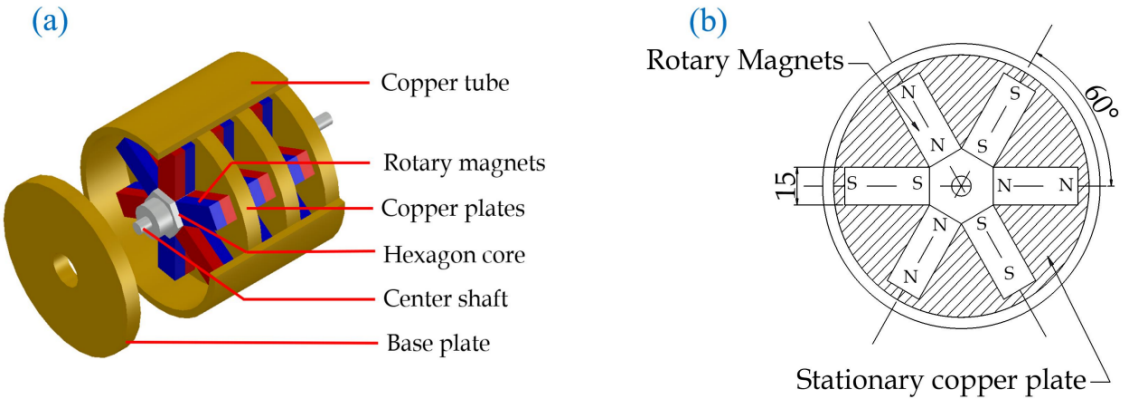

Fig. 3 Configuration of ECD-B: (a) 3D view and (b) cross-section view

Table 1 The parameters of ball screw, gearbox, and loading frame

Parameters	Value
Ball-screw lead (l)	16 mm
Ball-screw shaft diameter (D_s)	16 mm
Ball-screw design stroke	50 mm
Length of frame (L)	726 mm
Gearbox ratio (α)	8:1 (Setup II only)
Gearbox volume	3.47×10^4 mm^3 (Setup II only)

Table 2 Major parameters of ECDs

Parameters	ECD-A	ECD-B
Length (mm)	60	97
Outer diameter (mm)	110	120
Mass (kg)	5.6	5.4
Shaft diameter (mm)	8	8
Damper volume (mm^3)	5.70×10^5	1.10×10^6
No. of magnets	12	36
Volume of magnets (mm^3)	1.70×10^5	1.42×10^5

The major parameters of these setups are shown in Table 1, wherein the two setups have the same design parameters except the gearbox ratio. A large lead-to-diameter ratio (1:1 in this study) was selected to prevent the locking effect and minimize the friction. As aforementioned, when the gear ratio of 8 was used in Setup II, it is anticipated that the damping density would be amplified by 64 times.

It is noteworthy that the loading frame was designed to facilitate the installation on the testing machine. It is not a necessary part of the damper.

3. ECD

3.1 ECD Configurations

Inspired by Ellis *et al*. (1989), two configurations of rotary-type ECDs, namely, ECD-A and ECD-B, were designed, manufactured, and tested in this section. The schematics and photos of these two designs are shown in Figs. 2-4. As shown in Fig. 2, the ECD-A design comprises four concentric components, namely,

- An outer iron shell, which is an iron tube with the 110 mm outer diameter, 60 mm length, and 5 mm thickness;
- A middle magnet layer, which consists of 12 NdFeB magnets evenly distributed around a circle. The magnet

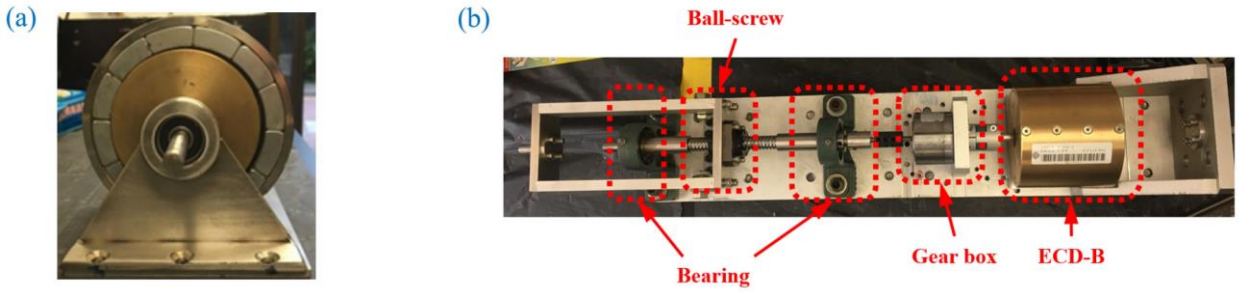

Fig. 4 Photos of ECDs: (a) cross-section of ECD-A, (b) configuration of ECD-B-II (with ball screw and gearbox)

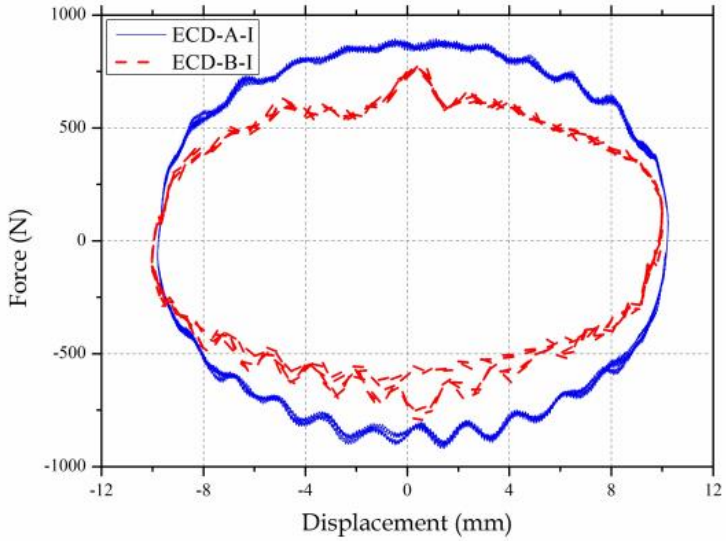

Fig. 5 The force-displacement relations of the ECD-A-I and ECD-B-I under cyclic loads (frequency f = 0.5 Hz, amplitude d = 10 mm)

poles were properly arranged as shown in Fig. 2. The thickness of each magnet is 10 mm;
- An inner solid core made of copper; and
- A central shaft with the 8 mm diameter. The shaft is supported on two bearings that are positioned by two steel supports on the base plate.

The magnetic layer is fixed on the outer shell, which forms a static part of the ECD-A design; whereas the copper core is mounted on the central shaft, which forms a rotating part of the ECD-A design. The air gap between the static and rotating parts is 1 mm.

Fig. 3 shows the schematic of the second design (i.e., the ECD-B design), whose configuration is different from that of the ECD-A design. The ECD-B configuration comprises the following major components:

- three coupled magnet layers, each of which consists of six pairs of NdFeB magnets evenly mounted on a hexagon core with an interval of 60°. The polarizations of the magnets are in the longitudinal direction of the damper;
- Four 10 mm thick copper plates, with two of them inserted between three magnet layers, and the other two serving as the cover plates of the ECD;
- A 8 mm diameter central shaft; and
- An outer shell with a diameter of 120 mm that houses all the components of the ECD-B design.

In the ECD-B design, the static part consists of the copper plates fixed on the outer shell, whereas the rotation part consists of three magnet layers mounted on the central shaft. The air gap between the magnetic layers and copper plates is 2 mm. All three layers of the magnets move at the same angular velocity and generate eddy currents in the adjacent copper plates.

The major parameters of ECD-A and ECD-B designs are summarized in Table 2. The rotary-type ECD (ECD-A or ECD-B) can be connected to the mechanical configurations described in Section 2 to form a complete ECD configuration. Different types of ECDs were

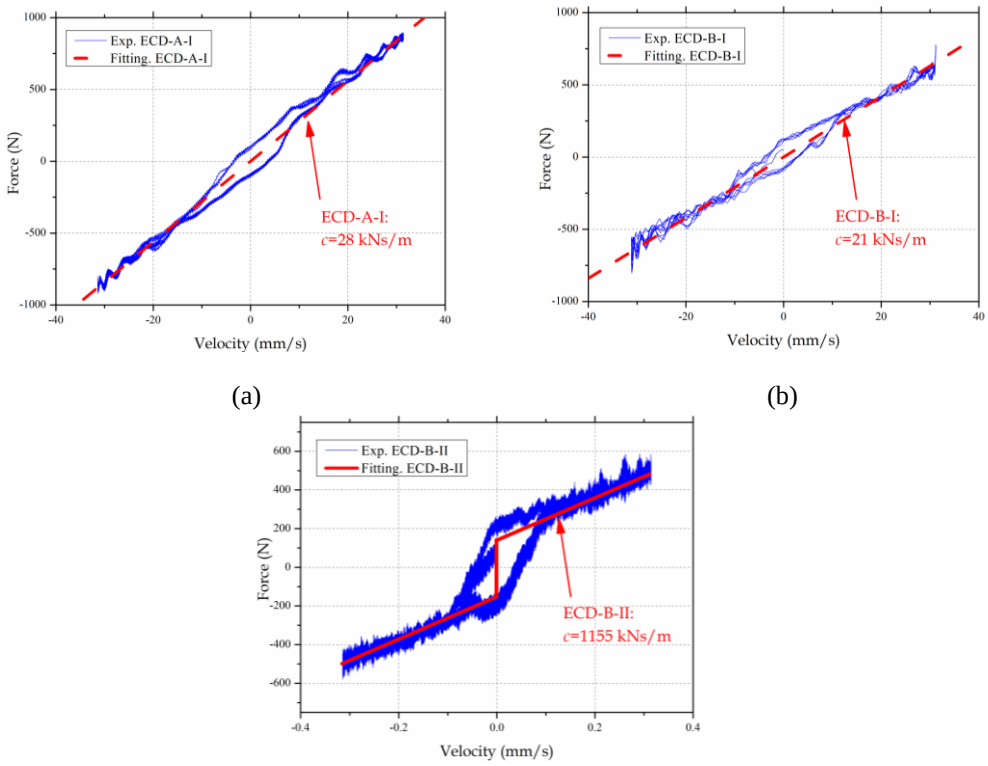

Fig. 6 Force-velocity relation of ECDs: (a) ECD-A-I under cyclic loads (f = 0.5 Hz, d = 10 mm), (b) ECD-B-I under cyclic loads (f = 0.5 Hz, d = 10 mm) and (c) ECD-B-II under cyclic loads (f = 0.005 Hz, d = 10 mm)

experimentally investigated in this section. They are referred to as ECD-A-I, ECD-B-I, and ECD-B-II, where ECD-A-I stands for the ECD-A design plus Setup I, ECD-B-I stands for the ECD-B design plus Setup I, and ECD-B-II stands for the ECD-B design plus Setup II.

3.2 Experimental results of ECD

The dampers ECD-A-I, ECD-B-I, and ECD-B-II were cyclically tested on an MTS universal testing machine with different loading conditions. Fig. 4(b) shows the photo of the ECD-B-II configuration tested in this study.

Fig. 5 shows the typical force–displacement relations of the ECD-A-I and ECD-B-I under harmonic loading with the frequency of 0.5 Hz and the displacement amplitude of 10 mm. Both configurations did not include the gear box. The larger peak damper force indicated that ECD-A-I is slightly more efficient than ECD-B-I.

Figs. 6(a)-6(c) shows the force–velocity relations of the ECD-A-I, ECD-B-I and ECD-B-II configurations, respectively, under cyclic loads. The ECD-A-I and ECD-B-I show nearly linear force-velocity relations. The eddy-current damping coefficients can be identified from the slopes of curves as 28 kNs/m and 21 kNs/m for ECD-A-I and ECD-B-I, respectively. The ECD-A-I provides a larger damping coefficient, even though its damper volume is less than that of ECD-B-I, as shown in Table 3. This finding indicates that 12 magnets that are placed seamlessly in ECD-A represent a more efficient arrangement in terms of magnet flux density.

Fig. 6(c) shows the force-velocity relation of the ECD-B-II configuration that includes a gearbox (α=8:1) in the design. Compared with Figs. 6(a) and 6(b), distinct friction effect can be identified in Fig. 6(c), which indicates that the use of the gearbox amplifies the friction effect in the whole system (for example, in the ball screw and gearbox components). Consequently, the total damping of the system is the superposition of the eddy-current damping and coulomb damping. Coulomb damping is non-viscous (i.e., rate-independent) damping, and the corresponding equivalent viscous damping coefficient can be computed based on an equal energy dissipation rule as

$$c_{\text{clmb}} = \frac{2F_{\text{fric}}}{\pi^2 fd} \tag{3}$$

where c_{clmb} is the equivalent damping coefficient of the coulomb damping, F_{fric} represents the magnitude of friction force, and f and d are the frequency and displacement amplitude of the oscillation, respectively. The friction force identified from Fig. 6(c) is around 0.16 kN, and the corresponding equivalent damping coefficient is c_{clmb} = 648 kNs/m.

The eddy-current damping coefficient of the ECD-B-II can be identified as 1155 kNs/m, based on the slope of the regression line. Consequently, the total damping coefficient can be calculated as

$$c_{\text{t}} = c_{\text{eddy}} + c_{\text{clmb}} \tag{4}$$

Fig. 7 The EMD tested on an MTS machine

where c_t denotes the total damping coefficient and c_{eddy} is the eddy-current damping coefficient. The major parameters identified from the experiments are summarized in Tables 3. The total damping coefficient (c_t) for the ECD-B-II is around 1803 kNs/m, in which the eddy current damping accounts for 64%.

3.3 Damping density of ECDs

The damping densities of ECDs are calculated according to Eq. (1). The volumes of ECD-A and ECD-B listed in Table 2, as well as the volume of the gearbox (if used), are counted in the total damper volume. It is noteworthy that the whole damper including the loading frame, long-stroke ball screw and bearings occupies more volume. However, these components were mainly designed to facilitate the installation and testing on the MTS machine, and are not regarded as compulsory parts of the ECD dampers. Their corresponding volumes can be considerably reduced by the optimization of the ECD structures, and are not considered in the damping density calculation. Thus, the calculated damping densities in this study represent the ideal damping densities that can be achieved in practice.

Notably, Shi and Zhu (2017) optimized the design of a linear-motion ECD, in which a cylindrical magnet moves linearly inside a copper tube, and obtained the optimal eddy-current damping density of 3.8 MNs/m^4 by considering the magnet volume only. This value drops to 0.117 MNs/m^4 when the volume of the copper tube is also considered.

Table 3 The experimental results of ECD tests

Parameters	ECD-A-I	ECD-B-I	ECD-B-II
EC damping c_{eddy} (kNs/m)	28	21	1155
Friction force, F_{fric} (kN)	NEGL.	NEGL.	0.16
Coulomb damping coefficient, c_{clmb} (kNs/m)	NEGL.	NEGL.	648
Total damping coefficient, c_t (kNs/m)	28	21	1803
Eddy-current damping density DD (MNs/m^4)	49.1	19.1	1018

* NEGL. stands for negligible

The calculated eddy-current damping densities in this study are summarized in Table 3. The damping densities obtained in this study are considerably higher: the eddy-current damping densities of the ECD-A-I and ECD-B-I are 420 and 163 times, respectively, to the optimal value reported by Shi and Zhu (2017). Compared with conventional linear-motion ECDs, the linear-to-rotary conversion in the current design can significantly enhance the damping efficiency, even without the gearbox (α=1).

Moreover, the use of the gearbox in the ECD-B-II can further enhance the damping density significantly. The achieved eddy-current damping density of the ECD-B-II is increased by 8701 times, compared with that for the linear-type ECD reported by Shi and Zhu (2017).

Both ECD-B-I and ECD-B-II adopt the same ECD-B design. Their comparison indicates that the ECD-B-II provides an eddy-current damping density 53 times that of

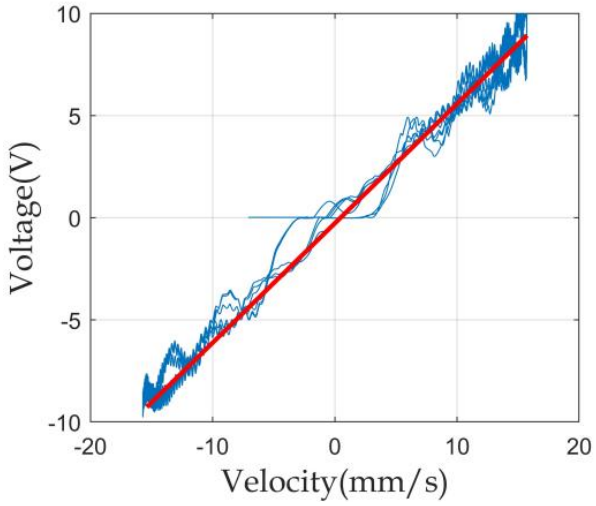

Fig. 8 The open-circuit voltage vs. damper velocity relation of the proposed EMD (blue thin line shows experimental results; red thick line shows the fitting curve)

the ECD-B-I. As far as the total damping coefficients are concerned, the amplification factor becomes 83 times. These results are very close to the theoretical prediction that a gearbox with a gear ratio α amplifies the damping by a factor of α^2.

These results reiterate the effectiveness of the two improvement measures, namely, the ball-screw plus the gearbox.

4. EMD

This section presents the design, principle, and experimental results of the improved EMD. The obtained damping density of the improved EMD design is compared with those of traditional linear-type EMDs reported in the literature.

4.1 Configuration of EMD

The proposed EMD system comprises the linear-to-rotary conversion setup II (i.e., the ball-screw + a gearbox) and an EM motor connected to the external circuit. It essentially replaces the ECD-B-II presented in the last section with a rotary EM motor. Fig. 7 shows a photo of the EMD tested on the MTS machines, with the annotations of different components. The linear motion of the MTS machine is converted by the ball screw to the rotary motion, then the rotary motion is accelerated by the gearbox before input to the EM motor – same mechanism as ECD-B-II. The rotary motion generates *emf* at two terminals of the EM motor. The whole EMD system satisfies the following relations

$$\begin{aligned} U &= K_{\text{em}}\dot{x} \\ F &= K_{\text{em}}I \end{aligned} \tag{5}$$

where U is the back *emf* (also known as open-circuit voltage) that is proportional to the linear velocity $\dot{x}$ of the damper, the damper force F is proportionally to the current I passing through the motor coil, and K_{em} is the motor constant that is an intrinsic property of an EMD system.

Fig. 8 shows the open-circuit voltage vs damper velocity relation of the tested EMD. According to Eq. (5), K_{em} = 640 N/A (or Ns/m) can be determined from the regression analysis, where the motor constant K_{em} is defined for the linear motion of the damper.

When the EM motor is connected to a pure resistor, it provides an EM damping coefficient as (Zhu *et al*. 2012)

$$c_{\text{em}} = \frac{K_{\text{em}}^2}{R_t} \tag{6}$$

where R_{t} is the total resistance of the circuit and c_{em} is the EM damping coefficient. A small R_{t} is desirable to achieve a large damping coefficient c_{em}. Without external facilitation, the maximum damping coefficient is capped by the internal coil resistance ($R_{\text{t}} = R_{\text{in}}$) when the EM motor is connected to a short circuit.

The major parameters of the EMD system are listed in Table 4. The motor inner resistance and inductance values are measured using an LCR meter (Model no. Hoiki 3522-50). The inner inductance of the EMD is typically ignorable under low-frequency excitations.

Table 4 Parameters of the tested EMD system

Parameter	Value
Motor constant (K_{em})	640 N/A
Motor inner resistance (R_{in})	12.4 Ω
Motor inner inductance (L_{in})	11.35 mH
Motor length	95 mm
Motor diameter	85 mm
Motor volume	5.39×10^{-4} m^3
Motor + gearbox volume	5.74×10^{-4} m^3
Motor weight	2.4 kg

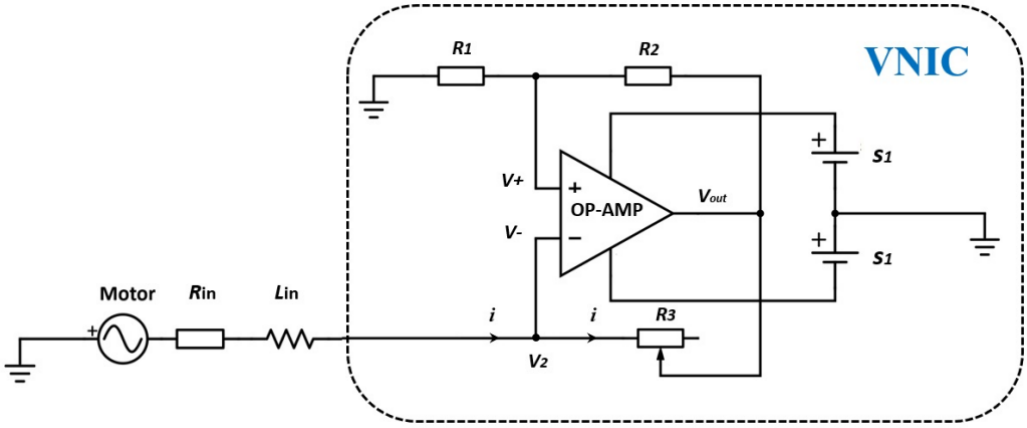

Fig. 9 EMD with a VNIC system (Li and Zhu 2018)

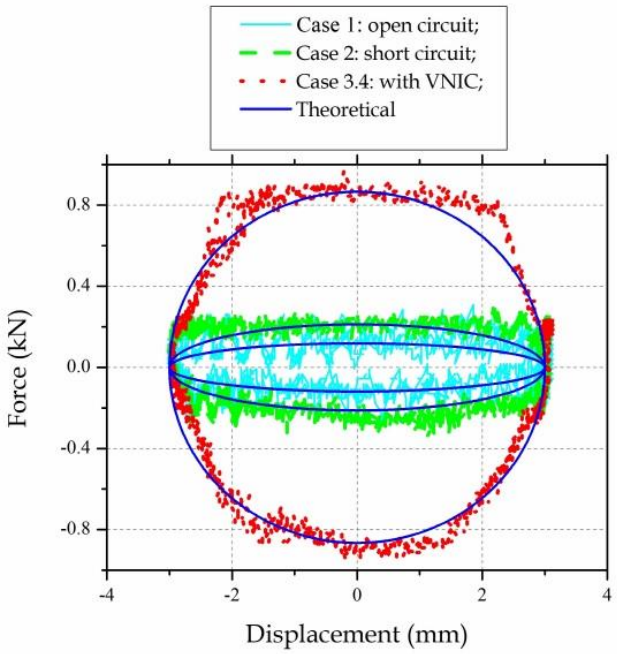

Fig. 10 Force–displacement relations of EMD within harmonic tests (f = 0.15 Hz, d = 3 mm)

Similar to the discussion in the last section, a gearbox can amplify the motor constant by a factor α; consequently, the achievable EM damping coefficient will be enhanced by an amplification factor of α^2.

4.2 VNIC

As aforementioned, the internal resistance R_{in} of the motor generally limits the maximum EM damping coefficient. However, Li and Zhu (2018) demonstrated that a negative impedance converter (NIC) with voltage inversion, termed VNIC, could partially offset the adverse impact of the internal resistance. VNIC, also known as a transconductance amplifier with a negative gain, functions essentially like a negative resistor. Thus, VNIC is introduced in this study as another improvement measure for the EMD, in addition to the ball-screw and gearbox.

Fig. 9 shows the schematic of VNIC, where the core component is a high-power operational amplifier whose function is controlled by three resistors (R_1~R_3). By adjusting the relative values of the resistors, the equivalent negative resistance can be determined as

$$R_{\mathrm{VNIC}} = -\frac{R_1 R_3}{R_2} \tag{7}$$

where R_{VNIC} is the equivalent negative resistance, and R_1, R_2, and R_3 are the resistance values of the resistors shown in Fig. 9. When R_1 and R_2 are equal, R_{VNIC} equals -R_3.

The use of VNIC aims to reduce the total resistance of the EMD, i.e., $R_t = R_{in} + R_{\mathrm{VNIC}} < R_{in}$. Consequently, according to Eq. (6), the EM damping coefficient of the EMD can be considerably increased. More details about VNIC, including the working mechanism and power

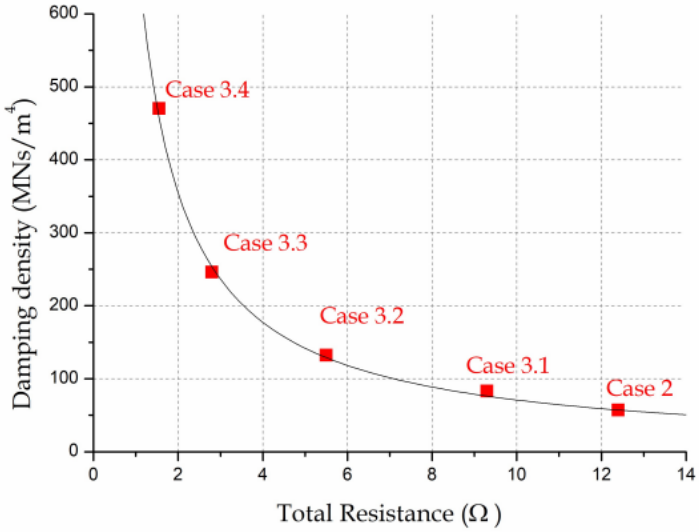

Fig. 11 EM damping density vs. total circuit resistance of the tested EMD-VNIC (solid line: theoretical curve; red square dot: experimental results)

consumption, can be found in the reference of Li and Zhu (2018).

In this study, R_1 and R_2 were both selected as 1 MΩ, and R_3 was initially set to be 10.85 Ω (Case 3.4). As a result, the total system resistance can be calculated as $R_t = R_{in} + R_{VNIC} =$ 1.55 Ω. R_3 value was varied during the tests later on.

4.3 Experimental results of EMD

Three test scenarios were conducted, including

- Case 1: open circuit (When the EMD was not connected to any circuit, $R_t = \infty$)
- Case 2: short circuit (When the output ends of the EMD were shorted, $R_t = R_{in}$=12.4 Ω)
- Case 3: EMD-VNIC (When the EMD was connected to VNIC, $R_t < R_{in}$). R_3 value was tuned during the test. Consequently, Case 3 contained several sub-cases:

Case 3.1: R_{VNIC} = -3.1 Ω, R_t = 9.3 Ω
Case 3.2: R_{VNIC} = -6.9 Ω, R_t = 5.5 Ω
Case 3.3: R_{VNIC} = -9.6 Ω, R_t = 2.8 Ω
Case 3.4: R_{VNIC} = -10.85 Ω, R_t = 1.55 Ω

Fig. 10 shows the typical force-displacement relations obtained in harmonic tests with a loading frequency of 0.15 Hz and a displacement amplitude of 3 mm.

In Case 1, the EM damping is zero, and the damping is mainly contributed by the coulomb damping. Referring to Fig. 10, the friction force can be identified around 98 N in Case 1, and the corresponding coulomb damping can be calculated as 44 kNs/m for the given frequency and amplitude according to Eq. (3).

Case 2 shows the combined effect of the coulomb and EM damping. The EM damping coefficient for Case II can be calculated as 33 kNs/m using Eq. (6), leading to an overall damping coefficient of 77 kNs/m. Notably, the contribution of the EM damping is less than the coulomb damping.

In Case 3, damping coefficient is enhanced by VNIC. For example, in Case 3.4, when R_{VNIC} = –10.85 Ω is connected, the EM damping is considerably increased to 264 kNs/m, leading to a total damping coefficient of 308 kNs/m.

Fig. 10 also shows the theoretical curves plotted on the basis of the estimated total damping coefficients. The good agreements between the theoretic and experimental curves justify the accuracy of the damping estimation.

4.4 Damping densities of EMDs

The damping densities of the EMDs are calculated based on the volumes of the rotary EM motor and the gearbox, by assuming that the volumes of the loading frame, shaft, and bearings can be minimized via further design optimization. Similar to Section 3.3, the presented damping densities represent ideal cases that can be achieved in practice. Furthermore, by removing the coulomb damping from the total damping, only the EM damping is considered in the calculation, as the coulomb damping is amplitude dependent.

As shown in Table 5, the EM damping densities contributed by the EM force are 0, 57 and up to 470 MNs/m^4 for the EMDs in Case 1, Case 2 and Case 3.4, respectively from the experiment results. The comparison between Case 2 and Case 3.4 highlights the effectiveness of the VNIC that enables 8 times increase in the EM damping density.

Fig. 11 shows the variation of the EM damping density with the total resistance of the circuit, in which the experimental cases are shown by red squares, and the

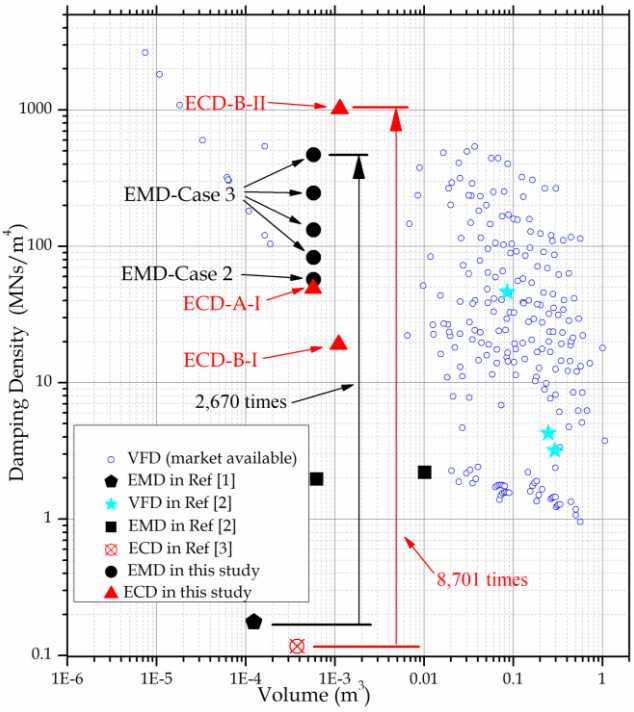

Fig. 12 Damping density vs. damper volume in log–log scale (Ref [1]: Zhu *et al*. (2012); Ref [2]: Palomera-Arias *et al*. (2008); Ref [3]: Shi and Zhu (2017))

Table 5 Parameters of the tested EMD-VNIC system

Parameter	Value
Device friction coefficient (F_{fric})	98 N
Coulomb damping coefficient (c_{clmb})	44 kNs/m
EM Damping density (Case 1)	0 MNs/m^4
EM Damping density (Case 2)	57 MNs/m^4
EM Damping density (Case 3.1)	83 MNs/m^4
EM Damping density (Case 3.2)	132 MNs/m^4
EM Damping density (Case 3.3)	246 MNs/m^4
EM Damping density (Case 3.4)	470 MNs/m^4

theoretical relation is based on Eq. (6). Satisfactory agreement between the experimental and theoretical results demonstrates the effectiveness of proposed VNIC in physical applications.

Palomera-Arias *et al*. (2008) numerically obtained a damping density of approximately 2 MNs/ m^4 for a linear-motion EMD adopting neodymium magnets (grade N35). Zhu *et al*. (2012) experimentally tested a conventional linear-motion EM damper, with a diameter of 38.1 mm and a length of 108.1 mm. The tested damper was essentially a small non-commutated moving magnet dc linear motor. The obtained maximum EM damping and total damping coefficients were around 14 Ns/m and 21.726 Ns/m, respectively, when the damper was cyclic tested (f=2 Hz, d=11 mm). Consequently, the corresponding damping density can be calculated as 0.176 MNs/m^4. A simple comparison illustrates a significant improvement in damping densities achieved by the proposed EMD-VNIC system whose damping density is 2670 times higher.

5. Damping density comparison with market-available VFDs

A parallel comparison with market available dampers is conducted to validate the efficiency of the proposed ECD and EMD prototypes and to shed light on future large-scale applications. The damping densities of 240 market-available VFDs from 15 different damper manufacturers are calculated and plotted against damper volume in Fig. 12. They are marked with light blue circles. Fig. 12 is plotted in a log–log scale. In general, small VFDs tend to possess high damping densities. However, large variability in damping densities can also be observed.

The damping densities of the tested ECDs and EMDs in this study are marked with solid red triangles and solid black circles, respectively, together with those of ECDs and EMDs reported in the literatures as shown in legend. In comparison with VFDs, the conventional linear-motion ECDs and EMDs typically have lower damping densities. However, with the multiple improvement measures proposed in this study, these improved versions of ECDs and EMDs possess damping densities comparable to (or even higher than) market-available VFDs. Moreover, the obtained damping densities of the proposed ECDs and EMDs cover a wide range, which offers flexibility in practical applications.

6. Conclusions

This study proposes the improved designs of ECDs and EMDs, aiming to enhance the damping densities of these two emerging dampers considerably. The adopted mechanical improvement measures include the use of the ball screw (linear-to-rotary motion conversion) and the gearbox. In addition, VNIC circuit is connected to the EMD to reduce the total resistance of the circuit. The design configurations and the experimental results are presented in details. The comparison results indicate that the proposed ECD and EMD designs can enhance the damping densities by several orders of magnitude. Their damping densities are comparable to (or even higher than) those of market-available VFDs. The promising results obtained in this study will shed light on the design and use of ECDs and EMDs as alternatives to commonly used VFDs. Large-scale compatibility of the proposed ECDs and EMDs will still deserve some future study.

Acknowledgements

The authors are grateful for the financial support from the Research Grant Council of Hong Kong through the NSFC/RGC Joint Research Scheme (N_PolyU533/17, 51761165022) and the Research Impact Fund (PolyU R5020-18). The findings and opinions expressed in this paper are solely those of the authors and not necessarily the views of the sponsors.

References

Bae, J.S., Kwak, M.K. and Inman, D.J. (2005), "Vibration suppression of a cantilever beam using eddy current damper", *J. Sound Vib.*, **284**(3-5), 805-824. https://doi.org/10.1016/j.jsv.2004.07.031.

Behrens, S., Fleming, A.J. and Moheimani, S.O.R. (2005), "Passive vibration control via electromagnetic shunt damping", *IEEE/ASME T. Mechatronics*, **10**(1), 118-122.

Behrens, S., Moheimani, S.O.R. and Fleming, A.J. (2003), "Multiple mode current flowing passive piezoelectric shunt controller", *J. Sound Vib.*, **266**(5), 929-942. https://doi.org/10.1016/S0022-460X(02)01380-9.

Cassidy, I.L., Scruggs, J.T., Behrens, S. and Gavin, H.P. (2011), "Design and experimental characterization of an electromagnetic transducer for large-scale vibratory energy harvesting applications", *J. Intel. Mat. Syst. Str.*, **22**(17), 2009-2024. https://doi.org/10.1177/1045389X11421824.

Ellis, R.C.C., Fink, R.A. and Rich, R.W. (1989), "Eddy Current Damper", *NASA, Marshall Space Flight Center, The 23rd Aerospace Mechanisms Symposium;*, Honeywell Space and Aviation Systems; Durham, NC, United States.

Fleming, A.J. and Moheimani, S.O.R. (2006), "Inertial vibration control using a shunted electromagnetic transducer", *IEEE/ASME T. Mechatronics*, **11**(1), 84-92. DOI: 10.1109/TMECH.2005.863364.

Heald, M.A. (1988), "Magnetic braking: Improved theory", *Am. J. Phys.*, **56**(6), 521-522. https://doi.org/10.1119/1.15570.

Housner, G., Bergman, L., Caughey, T., Chassiakos, A., Claus, R., Masri, S., Skelton, R., Soong, T., Spencer, B. and Yao, J. (1997), "Structural control: past, present, and future", *J. Eng. Mech.*, **123**(9), 897-971. https://doi.org/10.1061/(ASCE)0733-9399(1997)123:9(897).

Inoue, T., Ishida, Y. and Sumi, M. (2008), "Vibration suppression using electromagnetic resonant shunt damper", *J. Vib. Acoust.*, **130**(4), 41003. doi:10.1115/1.2889916.

Jamshidi, M., Chang, C.C. and Bakhshi, A. (2017), "Self-powered hybrid electromagnetic damper for cable vibration mitigation", *Smart Struct. Syst.*, **20**(3), 285-301. https://doi.org/10.12989/sss.2017.20.3.285.

Lee, K., and Park, K. (1999), "Optimal robust control of a contactless brake system using an eddy current." *Mechatronics*, *Pergamon*, **9**(6), 615-631.

Li, J.Y. and Zhu, S. (2018), "Versatile behaviors of electromagnetic shunt damper with a negative impedance converter", *IEEE/ASME T. Mechatronics*, **23**(3), 1415-1424. DOI: 10.1109/TMECH.2018.2813307.

Lu, X., Zhang, Q., Weng, D., Zhou, Z., Wang, S., Mahin, S.A., Ding, S. and Qian, F. (2017), "Improving performance of a super tall building using a new eddy-current tuned mass damper", *Struct.Control Health Monit.*, **24**(3), 1-17. https://doi.org/10.1002/stc.1882.

Nakamura, Y., Fukukita, A., Tamura, K., Yamazaki, I., Matsuoka, T., Hiramoto, K. and Sunakoda, K. (2014), "Seismic response control using electromagnetic inertial mass dampers", *Earthq. Eng. Struct. D.*, **43**(4), 507-527. https://doi.org/10.1002/eqe.2355.

Niu, H., Chen, Z., Hua, X. and Zhang, W. (2018), "Mitigation of wind-induced vibrations of bridge hangers using tuned mass dampers with eddy current damping", *Smart Struct. Syst.*, **22**(6), 727-741. https://doi.org/10.12989/sss.2018.22.6.727.

Palomera-Arias, R., Connor, J.J. and Ochsendorf, J.A. (2008), "Feasibility study of passive electromagnetic damping systems", *J. Struct. Eng.*, **134**(1), 164-170. https://doi.org/10.1061/(ASCE)0733-9445(2008)134:1(164).

Shen, W., Zhu, S. and Xu, Y. (2012), "An experimental study on self-powered vibration control and monitoring system using electromagnetic TMD and wireless sensors", *Sensor. Actuat. A Phys.*, **180**, 166-176. https://doi.org/10.1016/j.sna.2012.04.011.

Shen, W., Zhu, S., Xu, Y.L. and Zhu, H.P. (2018), "Energy regenerative tuned mass dampers in high-rise buildings", *Struct. Control Health Monit.*, **25**(2), 1-18. https://doi.org/10.1002/stc.2072.

Shen, W., Zhu, S., Zhu, H. and Xu, Y. L. (2016), "Electromagnetic energy harvesting from structural vibrations during earthquakes", *Smart Struct. Syst.*, **18**(3), 449-470. http://dx.doi.org/10.12989/sss.2016.18.3.449.

Shi, X. and Zhu, S. (2017), "Simulation and optimization of magnetic negative stiffness dampers", *Sensor. Actuat. A: Phys.*, **259**, 14-33. https://doi.org/10.1016/j.sna.2017.03.026.

Simeu, E. and Georges, D. (1996), "Modeling and control of an eddy current brake", *Control Eng. Pract.*, **4**(1), 19-26. https://doi.org/10.1016/0967-0661(95)00202-4.

Smith, M.C. (2002), "Synthesis of mechanical networks: the inerter", *IEEE T. Automat.Control*, **47**(10), 1648-1662. DOI: 10.1109/TAC.2002.803532.

Sodano, H.A. and Bae, J.S. (2004), "Eddy current damping in structures", *Shock Vib. Digest*, **36**, 469-478.

Sodano, H.A., Bae, J.S., Inman, D.J. and Belvin, W.K. (2005), "Concept and model of eddy current damper for vibration suppression of a beam", *J. Sound Vib.*, **288**(4-5), 1177-1196. https://doi.org/10.1016/j.jsv.2005.01.016.

Wang, Z., Chen, Z. and Wang, J. (2012), "Feasibility study of a large-scale tuned mass damper with eddy current damping mechanism", *J. Earthq. Eng. Eng. Vib.*, **11**(3), 391-401.

Wiederick, H.D., Gauthier, N., Campbell, D.A. and Rochon, P. (1987), "Magnetic braking: Simple theory and experiment", *Am. J. Phys.*, **55**(6), 500-503. https://doi.org/10.1119/1.15103.

Yan, B., Zhang, X. and Niu, H. (2012), "Vibration isolation of a beam via negative resistance electromagnetic shunt dampers", *J. Intel. Mat. Syst. Str.*, **23**(6), 665-673. https://doi.org/10.1177/1045389X12437889.

Zhu, H., Li, Y., Shen, W. and Zhu, S. (2019), "Mechanical and energy-harvesting model for electromagnetic inertial mass dampers", *Mech. Syst. Signal Pr.*, **120**, 203-220. https://doi.org/10.1016/j.ymssp.2018.10.023.

Zhu, S., Shen, W. and Xu, Y. (2012), "Linear electromagnetic devices for vibration damping and energy harvesting: Modeling and testing", *Eng. Struct.*, **34**, 198-212. https://doi.org/10.1016/j.engstruct.2011.09.024.